Improvement of axial excitation confinement in temporal focusing-based multiphoton microscopy via spatially modulated illumination

Chia-Yuan Chang[a] and Shean-Jen Chen[b,*]

aCenter for Micro/Nano Science and Technology, National Cheng Kung Univ., Tainan 701, Taiwan
bCollege of Photonics, National Chiao Tung Univ., Tainan 711, Taiwan

ABSTRACT

Conventional temporal focusing-based multiphoton excitation microscopy (TFMPEM) can offer widefield optical sectioning with an axial excitation confinement (AEC) of a few microns. Herein, a developed TFMPEM with a digital micromirror device (DMD), acting as the blazed grating for light spatial dispersion and simultaneous patterned illumination, has been extended to implement spatially modulated illumination at structured frequency and orientation. By implementing the spatially modulated illumination, the beam coverage at the back-focal aperture of the objective lens can be increased. As a result, the AEC can be condensed from 3.0 μm to 1.5 μm in full width at half maximum for a 2-fold enhancement. Furthermore, by using HiLo microscopy with two structured illuminations at the same spatial frequency but different orientation, biotissue images according to the structured illumination with condensed AEC is obviously superior in contrast and scattering suppression.

Keywords: Nonlinear microscopy; Three-dimensional microscopy; Multiphoton processes; Temporal focusing; digital micromirror device.

1. INTRODUCTION

Multiphoton excitation (MPE) using near-infrared wavelengths in the low-absorption spectral window is a powerful tool for generating fluorescence signals deep inside biological specimens [1,2]. With high excitation photon density achieved by high numerical aperture (NA) objective focusing, the nonlinear optical phenomenon occurs at the confined focal point at the micron/submicron range. Based on MPE, two-photon excited fluorescence (TPEF) microscopy can offer the advantages of natural optical sectioning, minimum invasiveness, low photobleaching, and deep penetration depth [3-6]. High spatial resolution and three-dimensional (3D) fluorescence images can be reconstructed using the three-axis point scanning mechanism [8,9]. Furthermore, the second harmonic generation (SHG) signal provides label-free imaging that can reveal highly polarizable molecules and non-centrosymmetric structures, such as collagen and myosin [10,11]. Accordingly, MPE microscopy with the TPEF and SHG is suitable for imaging thick biotissues and in vivo studies, including directly imaging the cortical vasculature in a mouse's brain [6], skin disease diagnosis [12], cellular structures of the retina [13], and neuronal activities [14]. However, the high frame rate needed for dynamic biological observation has motivated the development of MPE microscopy toward high-throughput configurations [8]. Temporal focusing-based multiphoton excitation microscopy (TFMPEM) provides direct widefield TPEF imaging [15-18], in which the diffraction element (e.g., a blazed grating) separates different spectral components of ultrashort laser pulses into different angles according to the diffraction equation and induces spatial dispersion that broadens the laser pulse width. In the so-called 4-*f* system setup, the diverse spectral components temporally overlap in phase only at the focal plane of the objective lens. In this manner, the shortest pulse width that is sufficient to excite the TPEF and SHG signals is reconstructed. The constructive interference condition of temporal focusing provides an axial excitation confinement (AEC) of a few microns according to the following system parameters, namely the laser pulse width, initial beam size, system magnification, and the NA of the objective [19]. The TFMPEM with the breakthrough approach of high-throughput illumination and detection capability [20] has been applied for fast Brownian motion tracking [18,21], widefield fluorescence lifetime imaging [22], and 3D neuronal activity observation [23]. Further, the fast-imaging ability of the TFMPEM has been integrated with holographic optical tweezers [24] and a large-area multiphoton-induced ablation technique [25], thereby evolving into a multifunctional system in which both capabilities are realized with the use of only a single objective.

* sheanjen@nctu.edu.tw; phone +886-6-3032121#57807; fax +886-6-3032535

Patterned illumination has also been integrated into the TFMPEM via an optical mask for passive lithographic microfabrication [26]. To this end, an active spatial light modulator or digital micromirror device (DMD) can be adopted for generating arbitrary illumination patterns by either phase modulation [17,27] or intensity modulation [28]. Alternatively, a phase contrast filter can be used to transform the phase mask into an intensity pattern for shaped excitation of cortical neurons [29]. Besides 3D fabrication and functional excitation, patterned illumination can also be employed to improve image contrast and quality. Various image reconstruction techniques have been developed and widely adopted for widefield imaging, including image deconvolution with the point spread function (PSF) of the optical system [30]. With a single spatial frequency sinusoidal pattern, a well axially resolved widefield image can be analyzed with only a few images at different phase shifts [31]. HiLo microscopy combines the high spatial frequency component from a high-pass filtered image with the low spatial frequency component from the demodulated information of a patterned illumination image to improve the contrast of reconstructed widefield images [32,33]. In doing so, widefield images with rejection of the out-of-focus background can be obtained/produced [32]. Structured illumination microscopy (SIM) utilizes the spatial frequency modulation technique instead of two objectives, one on each side of the specimen, for illumination and detection [36]. With this technique, the detection bandwidth of the objective is expanded to achieve super-resolution imaging [34,35]. Based on the nonlinear fluorescence response, nonlinear SIM (NSIM) can be implemented with higher-order spatial frequency modulation to further broaden the detection bandwidth of the objective [34]. Moreover, such structured illumination techniques for widefield imaging have been integrated with TFMPEM and applied to improve both axial and lateral resolution [37-39].

The widefield TFMPEM has only one line shape at the back-focal plane of the objective; hence, the effective NA for focusing efficiency is reduced, which means that the AEC is a few microns. Comparatively, line scanning TFMPEM has a uniformly circular beam profile that can achieve the same AEC as a point scanning microscope [40,41]. However, line scanning TFMPEM requires additional components and mechanisms to complete two-dimensional imaging. The patterned illumination also causes diffraction that would further modify the beam profile at the back-focal plane, which could improve the AEC. In this paper, a developed TFMPEM with a single DMD that functions as the blazed grating for light spatial dispersion and simultaneous patterned illumination [42] has been extended to implement spatially modulated illumination at structured frequency and orientation. Through this approach, the spatially modulated illumination via the DMD can be configured to improve the beam shape uniformity and enlarge the area coverage at the back aperture of the objective according to the overall distributions of spatial dispersion and pattern diffraction. First, the AEC of the TFMPEM would range from nearly −15% degradation to +18% enhancement using single sinusoidal-patterned illumination at different spatial frequencies and orientations. Then, with a multi-orientated and saturated sinusoidal pattern, the axial excitation profile could achieve 1.5 μm in full width at half maximum (FWHM), which is an enhancement of nearly +50% with respect to conventional TFMPEM. Patterns with the same spatial frequency at different orientations are demonstrated to have almost the same axial pattern contrast confinement, even with different axial excitation profiles for the thin specimen. However, if the adopted pattern were to have better AEC, the illumination pattern would have better contrast in the specimen due to reduced scattering from out-of-focus regions for thick, turbid specimens. With enhanced patterned illumination contrast, superior performance of the image reconstruction would result. Therefore, by using HiLo microscopy with two-structured illumination at the same spatial frequency but different orientations for the dense cerebellar cortex of a mouse, the biotissue image according to the structured illumination with focused AEC is obviously superior in contrast and scattering distortion.

2. SYSTEM SETUP AND CALIBRATION

2.1 Overall TFMPEM setup

Figure 1 shows a schematic diagram of the overall TFMPEM setup with a single DMD that functions as the blazed grating for spatial dispersion and simultaneous patterned illumination [42]. The ultrafast laser source is a Ti:Sapphire regenerative amplifier (Spitfire Pro XP, Spectra-Physics, USA) coupled with a Ti:Sapphire ultrafast oscillator (Tsunami, Spectra-Physics, USA) as the seed beam. The regenerative amplifier has a 10 kHz repetition rate with a center wavelength of 800 nm, and provides 400 μJ/pulse with a 90 fs pulse width. A combination of a half-wave plate (HWP) and polarization beam splitter (PBS) is adopted for power adjustment while maintaining horizontal polarization. The fast mechanical shutter (VS14S-2-ZM-0-R3, Uniblitz, USA) is open only when imaging is in progress to avoid unnecessary photobleaching. The DMD (DLP7000, Texas Instrument, USA) has a 0.7-inch illumination area and 1024 × 768 pixels in a diagonal micromirror array with 13.68 μm pitch size. The mechanical tilt angle of every micromirror element is

±12°, with + and − indicating reflecting (ON) and blocking (OFF) the incident laser beam, respectively. The structure of the DMD can be considered equivalent to a blazed grating with a blazed angle of 12°. Further, the 10th order diffraction of the ultrafast laser is adopted as the system beam, thereby approaching the maximum power set by the diffraction equation. The dispersion efficiency was verified as being equivalent to that when using the 1st order diffraction of a 517 lines/mm blazed grating [42]. Furthermore, the DMD can easily display 8-bit patterns via a high definition multimedia interface, and can also implement spatially modulated illumination in structured frequency and orientation; as such, it induces diverse diffraction effects in efficiency and orientation. Accordingly, the DMD in the system acts not only as a dispersion element for temporal focusing, but also as a spatially modulated illuminator with diffraction effect at the back-focal plane of objective, as shown in Fig. 1.

In the figure, L1 and L2 comprise the relay set, and together with L3 and the objective (UPlanSApo 60XW/NA 1.2, Olympus, Japan) form the 4-f system for temporal focusing excitation in an upright optical microscope (Axio Imager.A2m, Carl Zeiss, Germany). The TPEF and SHG signal are first filtered by the dichroic mirror and short-pass filter to remove the reflected excitation laser, and then imaged to the high-sensitivity EMCCD (iXon Ultra 897, Andor, UK) through the L3 imaging lens and an additional 2.5x camera adaptor. The EMCCD has 512×512 active pixels with a 16 μm pixel size and can be thermoelectrically cooled to −80 °C with air. It provides 16-bit digitization resolution and a maximum 17 MHz readout rate. In addition, 3D images can be acquired by controlling the motorized stage (H101A ProScan, Prior Scientific, UK) via the 3-axis encoder and fast piezo focusing stage (NanoScanZ 200, Prior Scientific, UK) with a maximum 200 μm traveling range. All peripheral instrument communication and control are operated via a high-speed data acquisition card (PCIe-7842R, National Instruments, USA) with Virtex-5 LX50 FPGA by custom-made LabVIEW program.

Figure 1. Optical setup of TFMPEM with the DMD functioning as dispersion and diffraction.

2.2 System performance and calibration

The DMD-based TFMPEM was found to have an AEC of around 3.0 μm by measuring the axial intensity profile of a 200 nm-thick thin film doped with Rhodamine 6G (R6G) dye and estimating the FWHM of the fitted intensity profile. The lateral resolution was determined to be 425 nm by measuring the PSF of the system by using 100 nm fluorescent beads (F8888, Thermo Fisher Scientific, USA) fixed in agarose gel. Further, the peak emission wavelength was found to be 514 nm, i.e. the system cutoff spatial frequency is 2.35 μm^{-1} at 514 nm as 1.51 μm^{-1} at 800 nm. To create sinusoidal illumination on the specimen with a specific spatial frequency via the DMD, the magnification ratio of the DMD to the EMCCD must be estimated. With the sinusoidal pattern acted on the DMD and the R6G TPEF image captured by the EMCCD, the magnification ratio of pixel$_{DMD}$/pixel$_{EMCCD}$ was calculated to be around 0.5. Furthermore, by imaging the

stage micrometer (#36-121, Edmund Optics Inc., USA), a single pixel$_{EMCCD}$ was estimated to represent 132 nm at the front-focal plane of the objective. Consequently, we can generate arbitrary spatial frequency sinusoidal patterned illumination on the specimen by the DMD according to:

$$p[m,n] = Q\left[\frac{255}{2}\left(1 + \cos\left(\frac{2\pi f_{DMD}}{n}m + \phi\right)\right)\right] \tag{1}$$

where f$_{DMD}$ equal to 15.2 μm^{-1} is the reciprocal of the pixel$_{DMD}$ of 132 nm $\times$ the magnification ratio of 0.5, ϕ is the phase term, and n is the number of pixels$_{DMD}$ used to form a sinusoidal period. The quantization function, Q, is used to quantize the pattern value to 8-bit gray scale.

3. EXPERIMENTAL RESULTS AND DISCUSSIONS

3.1 AECs by sinusoidal patterned illumination at different orientations

The DMD-based TFMPEM induces spatial dispersion by the DMD, which splits the spectral components of the ultrafast laser. Figure 2(a) shows the beam shape at the back-focal plane of the objective, in which the white-dotted circle shows the back aperture boundary of the objective. The line-shaped beam shows that the dispersion expansion is perpendicular to the optical axis due to the "ON" status of the DMD without any pattern; accordingly, the DMD simply functions as a blazed grating in this case. When diverse sinusoidal patterns at different spatial frequencies and orientations are sequentially applied, the DMD causes corresponding diffraction effects in efficiency and orientation. Figures 2(b)-2(d) show the beam shapes with four different spatial-frequency sinusoidal patterns (i.e. 0.63 μm^{-1}, 0.84 μm^{-1}, 1.09 μm^{-1}, and 1.90 μm^{-1} at the front-focal plane from left to right) at the orientations of 0°, 90°, and 135°, respectively. Herein, the orientation, θ, is defined as 0° when the pattern orientation is parallel to the +12° tilt direction of the micromirror array (i.e. the 0° orientation parallel to the dispersion direction), as shown in Fig. 1. Conversely, the 90° orientation is perpendicular to the dispersion direction. The 2nd and higher order harmonic pattern of the diffraction induced by the sinusoidal patterns via the DMD can be clearly seen and might be due to the pulse width modulation (PWM) used for the time-averaged grayscale pattern generation mechanism [43]. However, we noted that the overall modified beam shape at the back-focal plane including the dispersion expansion and the pattern-induced diffraction seriously affected the AEC profile. The AEC improvement is defined as:

$$AMC\ Improvement = \left(1 - \frac{AEC\ with\ pattern}{AEC\ w/o\ pattern}\right) \times 100\% \tag{2}$$

where "AEC w/o pattern" is the axial intensity profile in FWHM without a pattern applied to the DMD and all pixels are "ON". In contrast, "AEC with pattern" is the axial intensity profile in FWHM when the sinusoidal pattern is applied.

Figure 2(e) shows the AEC improvement curves as a function of the sinusoidal pattern with spatial frequency k$_p$ at 0°, 90°, and 135° orientations. The red-, green-, and blue-dotted lines with circle markers indicate sinusoidal patterns at 0° 90°, and 135° orientations, respectively. For the patterns at the 90° and 135° orientations, when the spatial frequency of the sinusoidal pattern increases at the front-focal plane and the 1st order diffraction beam emerges, the measured AEC is improved. However, when the spatial frequency increases, the 2nd and higher order terms are truncated by the limited size of the objective's back aperture, which disrupts the overall axial excitation profile. The maximum AEC improvement is achieved when the 2nd order diffraction beam fully leaves the back-aperture region and the spatial frequencies are located at around 0.63 μm^{-1} and 0.84 μm^{-1} for the 90° and 135° orientation sinusoidal patterns, respectively. However, the 1st order diffraction beam is also truncated by the boundary of the back aperture when higher spatial frequency is applied. Nevertheless, the axial excitation profile returns to its original profile when the 1st order diffraction beam also moves away from the back-aperture region. As such, the pattern contrast at the front-focal plane of the objective nearly disappears because it approaches the measured spatial frequency cutoff of the system, which marks the detection limit of the system. On the other hand, for patterns at 0° orientation, the pattern-induced diffraction direction is the same as the dispersion direction. Consequently, the beam shape is the convolution of the dispersion-line shape and the diffraction profile of the sinusoidal pattern. It should be noted that the convolution is equivalent to the Fourier transform of the product of the DMD structure multiplied by the sinusoidal pattern [44]. The resulting line-shape beam has the most uniform intensity distribution when the 1st order diffraction is located at half of the cutoff spatial

frequency, which is around 1.09 μm^{-1} at 0° orientation. In this manner, the maximum AEC improvement of +18% can be obtained, as opposed to –11% for the same spatial frequency of 1.09 μm^{-1} at the 90° orientation.
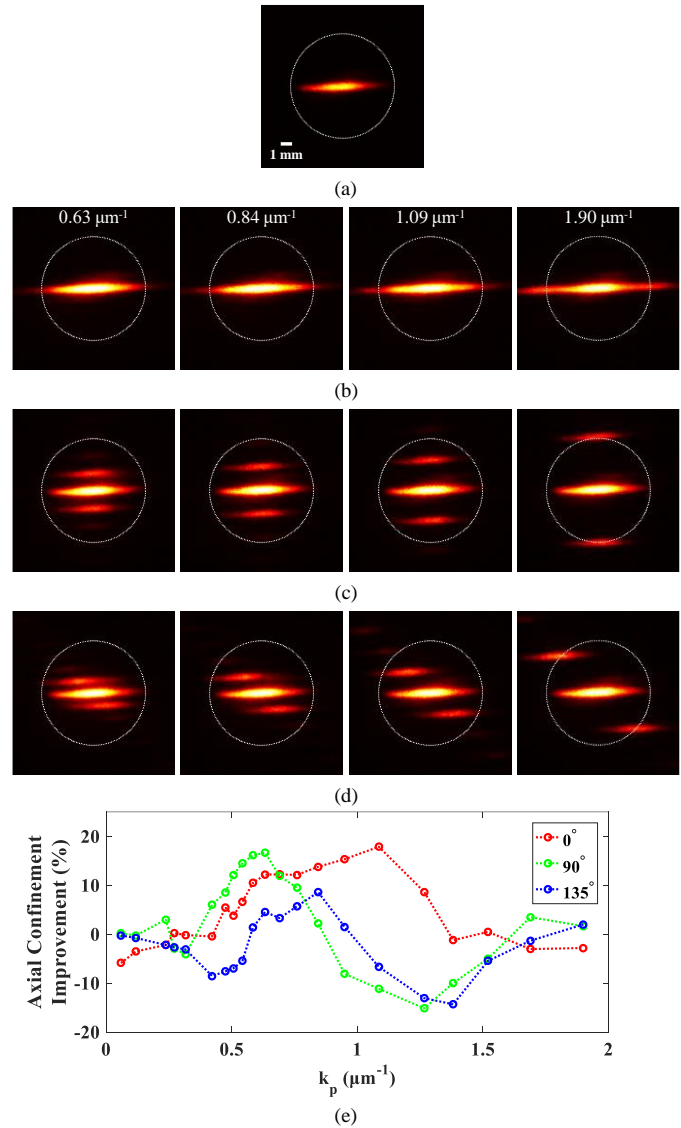

Fig. 2. Beam shapes at the back-focal plane of the objective, where the white dotted circle indicates the boundary of the objective aperture. (a) The beam shape without applied pattern and with all DMD pixels "ON". Four sinusoidal patterns with spatial frequencies k_p of 0.63 μm^{-1}, 0.84 μm^{-1}, 1.09 μm^{-1}, and 1.90 μm^{-1} (from left to right) are applied to the DMD at (b) 0° orientation, (c) 90° orientation, and (d) 135° orientation. (e) AEC improvement curves as a function of spatial frequency. Red, green, and blue curves indicate 0°, 90°, and 135° orientations, respectively.

To further extend the uniformity and coverage of the beam shape at the back-focal plane of the objective for superior AEC, we apply the saturated pattern on the DMD superposed with sinusoidal patterns at four different orientations as:

$$p_{4orient,\,saturated}[m] = 255 - Q\Big[\,Q\big[\,p_{0°}[m,n_2] + p_{90°}[m,n_2]\,\big] - Q\big[\,p_{45°}[m,n_3] + p_{135°}[m,n_3]\,\big]\,\Big] \tag{3}$$

where n_2 and n_3 are 24 and 18 which respectively indicate spatial frequencies of 0.63 μm^{-1} and 0.84 μm^{-1}. The spatial frequencies at a 90° orientation and both diagonal orientations (i.e. 45° and 135°) were chosen according to where Fig. 2(e) indicates the maximum improvement occurs. At the 0° orientation, we select the same spatial frequency as at the 90° orientation to further enhance the diffraction efficiency where the maximum improvement at the diagonal orientations occurs. Since we have superposed the four patterns at the four different orientations, we have to subtract 255 to reduce

the intensity of the zero order beam in the middle of the objective's back aperture. The resulting beam shape at the back-focal plane of the objective is shown in Fig. 3(a) and the corresponding TPEF patterned image at the front-focal plane is presented in Fig. 3(b). The corresponding axial excitation profile is the red curve shown in Fig. 3(c) and the estimated AEC in FWHM is 1.5 µm. The blue curve is the axial excitation profile without a pattern, for which the AEC improvement reaches 50%, which is almost a 2-fold enhancement.

(a)

(b)

(c)
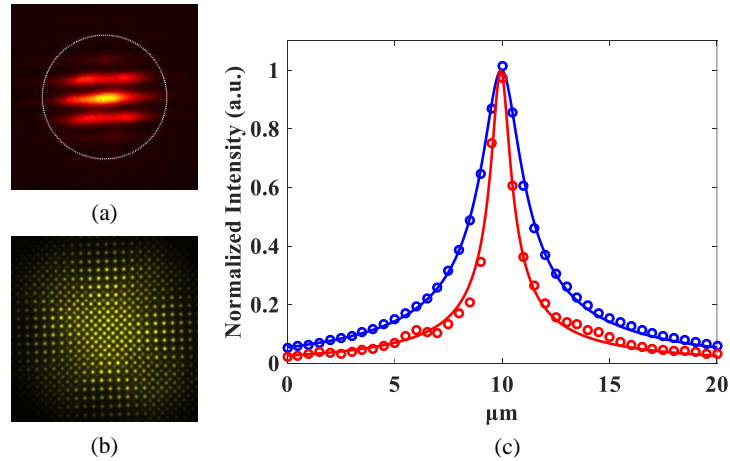
Fig. 3 (a) The beam shape at the back aperture of the objective. (b) The TPEF image of the saturated pattern described in Eq. (5) with superposition of the four sinusoidal patterns at the four different orientations at the front-focal plane. (c) Axial excitation profiles without a pattern and all DMD pixels "ON" (blue) and with the pattern shown in Fig. 3(a) (red). The circles are the average intensity of the images at different depths, and the solid lines are the fitted curves. The estimated AECs in FWHM are around 3.0 µm (blue) and 1.5 µm (red).

3.2 HiLo images of biotissue with different patterns

We have demonstrated that the AEC varies according to different patterns in spatial frequency and orientation via the DMD. However, the axial image resolution of TFMPEM is based on two major parts. The first is the AEC, which is related to the excitation wavelength and spectral components of the light source, the back-focal plane filling, the NA of the objective, and the dispersion distortion of the spectral components in the excitation optical path. The second part is the emission collection capability, which is dependent upon the emission wavelength of the sample, the NA of the objective, and the optical aberration in the collection optical path. To isolate the second issue for evaluating the axial image resolution of TFMPEM, the R6G thin film was excited with patterns at different spatial frequencies and orientations, after which TPEF images were taken axially. The specimen is only about 200 nm thick, so the scattering effect could be neglected; consequently, the contrast of the excited pattern is affected only by the emission collection capability, not the AEC. Herein, the sinusoidal intensity profiles of the TPEF patterned images at different depths are plotted via movement of the z-axis piezo stage. Then, the pattern contrast value of every patterned TPEF image is defined by measuring the root mean square (rms) value of the difference between the upper and lower envelopes of the sinusoidal intensity profile. Finally, the resulting axial pattern-contrast-value curves are fitted with the Gaussian function to define the axial pattern-contrast confinement by estimating the FWHM value. Figure 4(a) plots the axial pattern-contrast confinement with different spatial frequency patterns. The red, green, and blue circles indicate 0°, 90°, and 135° orientations. The axial pattern-contrast confinement increases as the spatial frequency increased. For the patterned excitation at the same spatial frequency, although the axial pattern-contrast confinements are consistent for the three orientations, they result in different AECs, as was shown in Fig. 2(e). This means that the emission collection capabilities of the current DMD-based TFMPEM are almost identical for the patterned excitations with the same spatial frequency but different orientations. However, in a thick specimen, the pattern contrast would be distorted due to the larger excitation volume inducing more scattering. Herein, a thick eosin-stained mouse cerebellar cortex specimen is imaged for demonstration. Figures 4(b) and (c) show the TPEF images of the biotissue at 17 µm under the surface (i.e. at a 17 µm depth) with the 1.09 µm^{-1} spatial frequency pattern at 90° and 0° orientations, respectively. Recall that the AEC improvements of the 1.09 µm^{-1} spatial frequency pattern at the 90° and 0° orientations in Fig. 2(e) are −11% and +18%, respectively. Although the TPEF images can still be acquired, the pattern at the 90° orientation (Fig. 4(b)) is difficult to recognize compared to the pattern with the same spatial frequency at the 0° orientation (Fig. 4(c)). The inferior AEC in Fig 4(b) displays larger scattering distortion in the dense specimen. Therefore, the excited pattern shows good contrast only at confined areas in condensed regions at depth.
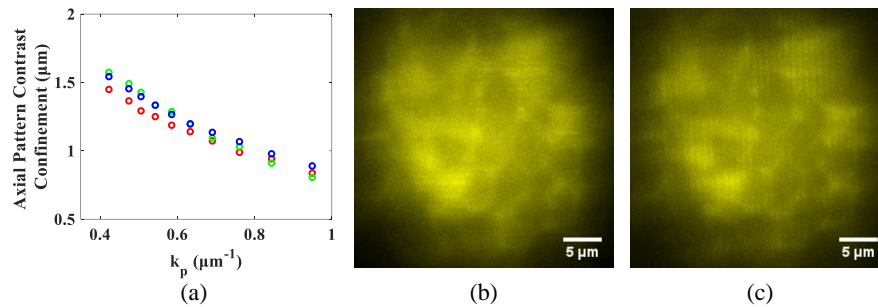
Fig. 4. (a) Axial pattern-contrast confinements with different spatial frequency patterns. The red, green, and blue circles are at 0°, 90°, and 135° orientations, respectively. The TPEF images of the eosin-stained mouse cerebellar cortex with 1.09 μm^{-1} spatial frequency pattern at (b) 90° and (c) 0° orientations at a 17 μm depth.

Moreover, the TPEF pattern contrast is important since many structured illumination techniques based on the pattern purity must have low noise and non-distorted image information modulation. The SIM and NSIM require several pattern images at different orientations with phase shifts for super-resolution image reconstructions [34,39]. Accordingly, these techniques should consider whether the differences among the AECs are nearly the same for the scatter-inducing specimen in the event that serious scattering occurs at certain orientations. If so, then every filter parameter and weighting must be adjusted in very specific detail during the reconstruction algorithm computation. The HiLo technique requires the in-focal-plane high-frequency component from the original image via a suitable high-pass filter; meanwhile, the in-focal-plane low-frequency component could be retrieved from the spatial-frequency modulated image by high-pass filtering, demodulation, and then low-pass filtering [32,33]. Figure 5(a) shows the original TPEF image of the eosin-stained mouse cerebellar cortex via the TFMPEM. The HiLo images are presented in Figs. 5(b) and (c), with the low-frequency components retrieved from the 1.09 μm^{-1} spatial frequency pattern images at 90° and 0° orientations, respectively. Although both HiLo images have the same high-frequency components from Fig 6(a), differences can still be seen in Figs. 5(b) and (c) since the 0°-orientation pattern has a superior AEC such that the scattering is reasonably reduced and the modulated information is less distorted. Therefore, the low-frequency component could be retrieved with less noise from the patterned image with the higher pattern contrast and less scattering distortion from the out-of-focus excitation region. Figure 5(d) shows the intensity profiles of the white-dotted lines in Figs. 5(a), (b), and (c). The blue curve is the original TPEF image, while the green and red curves are based on the HiLo images at the 90°- and 0°-orientation patterns, respectively. Although both HiLo images successfully reduced the background noise, the 0°-orientation offered better pattern contrast, and so is less blurry than that with the 1.09 μm^{-1} spatial frequency pattern at 90° orientation.
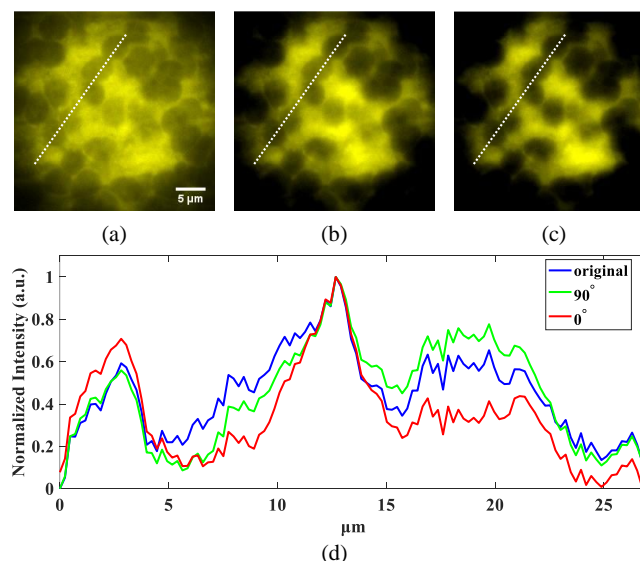

Fig. 5. (a) The original TPEF image of the eosin-stained mouse cerebellar cortex. The HiLo images with the low-frequency component analyzed with the 1.09 μm-1 spatial frequency pattern images at (b) 90° and (c) 0° orientations. (d) The intensity profiles of white dotted lines in Figs. 6(a) (blue), 6(b) (green), and 6(c) (red).

4. CONCLUSIONS

TFMPEM provides widefield TPEF images with natural optical sectioning ability and has the potential for fast volumetric imaging to monitor dynamic events in 3D. Integrated with patterned illumination, the system could further be applied for functional excitation, 3D fabrication, and structured illumination purposes. In this paper, we have demonstrated that the AEC would vary with different patterns at the same single spatial frequency and different orientations, and could reach over 30% difference, e.g. from –11% to +18% from 1.09 μm^{-1} spatial frequency patterns at the 90° and 0° orientations. In order to have a uniform beam shape at the back-focal aperture of the objective with less diffraction components truncated by the boundary, the saturated pattern combined with two spatial frequencies or multi-orientations could be applied for excitation. In this manner, the FWHM of the axial excitation profile could reach 1.5 μm from 3.0 μm, which is a 2-fold enhancement. By implementing the spatially modulated illumination, the beam coverage at the back-focal aperture of the objective lens was enlarged and the AEC remarkably improved.

Furthermore, the sinusoidal patterns with different spatial frequencies were shown to have almost the same axial contrast confinement at different orientations. The patterned excitation in the specimen might be distorted since the scattering results from a large axial excitation volume compared with the same spatial frequency patterns at different orientations, despite the pattern contrasts being shown to be approximately the same. We also compared the HiLo images using the patterns with the same spatial frequency, but at different orientations. The in-focal-plane low-frequency components of the HiLo analyzed from the two different patterns (i.e. 1.09 μm^{-1} spatial frequency patterns at the 90° and 0° orientations) revealed that the higher the sinusoidal pattern modulation purity is, the lower the background noise and the easier the parameters are to adjust during computation. It is noted, however, that the axial excitation profile might be further improved with adaptive optics to eliminate the dispersion induced in the specimen [45]. Saturated patterns with a 50% improved axial excitation profile are also possible for uniform widefield illumination by combining two, or several, saturated patterns with the assistance of the fast pattern-switching ability of the DMD. Finally, by using HiLo microscopy with the two structured illuminations, the biotissue image according to the structured illumination with condensed AEC was obviously superior in contrast and scattering suppression.

FUNDING

REFERENCES

[1] R. Weissleder, "A clearer vision for *in vivo* imaging," Nat Biotechnol. **19**(4), 316–317 (2001).
[2] T. G. Phan and A. Bullen, "Practical intravital two-photon microscopy for immunological research: faster, brighter, deeper," Immunol. Cell Biol. **88**(4), 438–444 (2010).
[3] W. Denk, J. H. Strickler, and W. W. Webb, "Two-photon laser scanning fluorescence microscopy," Science **248**(4951), 73–76 (1990).
[4] W. R. Zipfel, R. M. Williams, and W. W. Webb, "Nonlinear magic: multiphoton microscopy in the bioscience," Nat. Biotechnol. **21**(11), 1369–1377 (2003).
[5] F. Helmchen and W. Denk, "Deep tissue two-photon microscopy," Nat. Methods **2**(12), 932–940 (2005).
[6] D. Kobat, N. G. Horton, and C. Xu, "*In vivo* two-photon microscopy to 1.6-mm depth in mouse cortex," J. Biomed. Opt. **16**(10), 106014 (2011).
[7] E. E. Hoover and J. A. Squier, "Advances in multiphoton microscopy technology," Nat. Photonics **7**(2), 93–101 (2013).
[8] P. T. C. So, E. Y. S. Yew, and C. Rowlands, "High-throughput nonlinear optical microscopy," Biophys. J. **105**(12), 2641–2654 (2013).
[9] B. R. Masters and P. T. So, ed., *Handbook of Biomedical Nonlinear Optical Microscopy* (Oxford University Press, 2008).
[10] P. J. Campagnola and L. M. Loew, "Second-harmonic imaging microscopy for visualizing biomolecular arrays in cells, tissues and organisms," Nature Biotech. **21**(11), 1356–1360 (2003).
[11] F. S. Pavone and P. J. Campagnola, ed., *Second Harmonic Generation Imaging* (CRC Press, 2013).

[12] S.-Y. Chen, S.-U. Chen, H.-Y. Wu, W.-J. Lee, Y.-H. Liao, and C.-K. Sun, "*In vivo* virtual biopsy of human skin by using noninvasive higher harmonic generation microscopy," IEEE J. Sel. Top. Quantum Electron. **16**(3), 478–492 (2010).

[13] M. Han, G. Giese, S. Schmitz-Valckenberg, A. Bindewald-Wittich, F. G. Holz, J. Yu, J. F. Bille, and M. H. Niemz, "Age-related structural abnormalities in the human retina-choroid complex revealed by two-photon excited autofluorescence imaging," J. Biomed. Opt. **12**(2), 024012 (2007).

[14] C. Stosiek, O. Garaschuk, K. Holthoff, and A. Konnerth, "*In vivo* two-photon calcium imaging of neuronal networks," Proc. Natl. Acad. Sci. U. S. A. **100**(12), 7319–7324 (2003).

[15] D. Oron, E. Tal, and Y. Silberberg, "Scanningless depth-resolved microscopy," Opt. Express **13**(5), 1468–1476 (2005).

[16] G. Zhu, J. V. Howe, M. Durst, W. Zipfel, and C. Xu, "Simultaneous spatial and temporal focusing of femtosecond pulses," Opt. Express **13**(6), 2153–2159 (2005).

[17] O. D. Therrien, B. Aubé, S. Pagés, P. De Koninck, and D. Côté, "Wide-field multiphoton imaging of cellular dynamics in thick tissue by temporal focusing and patterned illumination," Biomed. Opt. Express **2**(3), 696–704 (2011).

[18] L.-C. Cheng, C.-Y. Chang, C.-Y. Lin, K.-C. Cho, W.-C. Yen, N.-S. Chang, C. Xu, C. Y. Dong, and S.-J. Chen, "Spatiotemporal focusing-based widefield multiphoton microscopy for fast optical sectioning," Opt. Express **20**(8), 8939–8948 (2012).

[19] H. Dana and S. Shoham, "Numerical evaluation of temporal focusing characteristics in transparent and scattering media," Opt. Express **19**(6), 4937–4948 (2011).

[20] C. G. Durfee and J. A. Squier, "Breakthroughs in photonics 2014: spatiotemporal focusing: advances and applications," IEEE Photon. J. **7**(3), 0700806 (2015).

[21] C.-Y. Chang, Y. Y. Hu, C.-Y. Lin, C.-H. Lin, H.-Y. Chang, S.-F. Tsai, T.-W. Lin, and S.-J. Chen, "Fast volumetric imaging with patterned illumination via digital micro-mirror device-based temporal focusing multiphoton microscopy," Biomed. Opt. Express **7**(5), 1727–1736 (2016).

[22] H. Choi, D. S. Tzeranis, J. W. Cha, P. Clémenceau, S. J. de Jong, L. K. van Geest, J. H. Moon, I. V. Yannas, and P. T. So, "3D-resolved fluorescence and phosphorescence lifetime imaging using temporal focusing wide-field two-photon excitation," Opt. Express **20**(24), 26219–26235 (2012).

[23] T. Schrödel, R. Prevedel, K. Aumayr, M. Zimmer, and A. Vaziri, "Brain-wide 3D imaging of neuronal activity in *Caenorhabditis elegans* with sculpted light," Nat. Methods **10**(10), 1013–1020 (2013).

[24] R. Spesyvtsev, H. A. Rendall, and K. Dholakia, "Wide-field three-dimensional optical imaging using temporal focusing for holographically trapped microparticles," Opt. Lett. **40**(21), 4847–4850 (2015).

[25] C.-Y. Lin, P.-K. Li, L.-C. Cheng, Y.-C. Li, C.-Y. Chang, A.-S. Chiang, C. Y. Dong, and S.-J. Chen, "High-throughput multiphoton-induced three-dimensional ablation and imaging for biotissues," Biomed. Opt. Express **6**(2), 491–499 (2015).

[26] D. Kim and P. T. C. So, "High-throughput three-dimensional lithographic microfabrication," Opt. Lett. **35**(10), 1602–1604 (2010).

[27] E. Papagiakoumou, V. de Sars, D. Oron, and V. Emiliani, "Patterned two-photon illumination by spatiotemporal shaping of ultrashort pulses," Opt. Express **16**(26), 22039–22047 (2008).

[28] Y.-C. Li, L.-C. Cheng, C.-Y. Chang, C.-Y. Lin, N.-S. Chang, P. J. Campagnola, C. Y. Dong, and S.-J. Chen, "High-throughput fabrication of gray-level bio-microstructures via temporal focusing excitation and laser pulse control," J. Biomed. Opt. **18**(7), 075004 (2013).

[29] E. Papagiakoumou, F. Anselmi, A. Bègue, V. de Sars, J. Glückstad, E. Y. Isacoff, and V. Emiliani, "Scanless two-photon excitation of channelrhodopsin-2," Nat. Methods **7**(10), 848–854 (2010).

[30] P. Sarder and A. Nehorai, "Deconvolution methods for 3-D fluorescence microscopy images," IEEE Sig. Proc. Mag. **23**(3), 32–45 (2006).

[31] M. A. A. Neil, R. Juskaitis, and T. Wilson, "Method of obtaining optical sectioning by using structured light in a conventional microscope," Opt. Lett. **22**(24), 1905–1907 (1997).

[32] J. Mertz and J. Kim, "Scanning light-sheet microscopy in the whole mouse brain with HiLo background rejection," J. Biomed. Opt. **15**(1), 016027 (2010).

[33] S. Santos, K. K. Chu, D. Lim, N. Bozinovic, T. N. Ford, C. Hourtoule, A. C. Bartoo, S. K. Singh, and J. Mertz, "Optically sectioned fluorescence endomicroscopy with hybrid-illumination imaging through a flexible fiber bundle," J. Biomed. Opt. **14**(3), 030502 (2009).

[34] M. G. L. Gustafsson, "Nonlinear structured-illumination microscopy: wide-field fluorescence imaging with theoretically unlimited resolution," Proc. Natl. Acad. Sci. U. S. A. **102**(37), 13081–13086 (2005).

[35] L. Schermelleh, P. M. Carlton, S. Haase, L. Shao, L. Winoto, P. Kner, B. Burke, M. C. Cardoso, D. A. Agard, M. G. L. Gustafsson, H. Leonhardt, and J. W. Sedat, "Subdiffraction multicolor imaging of the nuclear periphery with 3D structured illumination microscopy," Science **320**(5881), 1332–1336 (2008).

[36] M. G. L. Gustafsson, D. A. Agrad, and J. W. Sedat, "I^{5}M: 3D widefield light microscopy with better than 100 nm axial resolution," J. Microsc. **195**(1), 10–16 (1999).

[37] H. Choi, E. Y. S. Yew, B. Hallacoglu, S. Fantini, C. J. R. Sheppard, and P. T. C. So, "Improvement of axial resolution and contrast in temporally focused widefield two-photon microscopy with structured light illumination," Biomed. Opt. Express **4**(7), 995–1005 (2013).

[38] K. Isobe, T. Takeda, K. Mochizuki, Q. Song, A. Suda, F. Kannari, H. Kawano, A. Kumagai, A. Miyawaki, and K. Midorikawa, "Enhancement of lateral resolution and optical sectioning capability of two-photon fluorescence microscopy by combining temporal-focusing with structured illumination," Biomed. Opt. Express **4**(11), 2396–2410 (2013).

[39] L.-C. Cheng, C.-H. Lien, Y. D. Sie, Y. Y. Hu, F.-C. Chien, C. Xu, C. Y. Dong, and S.-J. Chen, "Nonlinear structured-illumination enhanced temporal focusing multiphoton microscopy with a digital micromirror device," Biomed. Opt. Express **5**(8), 2526–2536 (2014).

[40] M. E. Durst, G. Zhu, and C. Xu, "Simultaneous spatial and temporal focusing in nonlinear microscopy," Opt. Commun. **281**(7), 1796–1805 (2008).

[41] A. Vaziri and C. V. Shank, "Ultrafast widefield optical sectioning microscopy by multifocal temporal focusing," Opt. Express **18**(19), 19645–19655 (2010).

[42] J.-N. Yih, Y. Y. Hu, Y. D. Sie, L.-C. Cheng, C.-H. Lien, and S.-J. Chen, "Temporal focusing-based multiphoton excitation microscopy via digital micromirror device," Opt. Lett. **39**(11), 3134–3137 (2014).

[43] D. Dudley, W. Duncan, and J. Slaughter, "Emerging digital micromirror device (DMD) applications," Proc. SPIE **4985**, 14–25 (2003).

[44] J. W. Goodman, *Introduction to Fourier Optics*, 3rd ed. (Roberts and Company, 2005).

[45] C.-Y. Chang, L.-C. Cheng, H.-W. Su, Y. Y. Hu, K.-C. Cho, W.-C. Yen, C. Xu, C. Y. Dong, and S.-J. Chen, "Wavefront sensorless adaptive optics temporal focusing-based multiphoton microscopy," Biomed. Opt. Express **5**(6), 1768–1777 (2014).